

ALBIUS REPORT

JBO/Manchester: Paul Harrison (PAH), Simon Garrington (STG), Rob Beswick (RJB). Anita Richards (AMSR), Tom Muxlow (TWBM), Nick Wrigley (NW), Roger Noble (RGN)

ESO: Robert Laing (RL), Dirk Petry (DP)

1. Introduction

1.1 Direction dependent calibration at cm and mm wavelengths

In general, observations made with radio interferometers will be corrupted by a variety of telescope-based errors, arising in the telescope itself, the receiver and electronics, or in the atmosphere/ionosphere above the telescope. Until recently, most calibration approaches assumed that the errors were direction-independent, at least over the instantaneous field of view of the instrument, which allows the calibration and imaging steps to be considered separately. The new generation of radio interferometers (EVLA, e-MERLIN, EVN, LOFAR, ALMA) are now being pushed to wider fields of view, lower frequencies and higher sensitivities/dynamic ranges so that direction-dependent errors must also be taken into account. The most important terms are the phase variations due to ionospheric structure at low frequencies and the beam-response of each individual telescopes, which are dominant at higher frequencies. At very low frequencies, the direction dependent effects of the ionosphere become important, and these are discussed elsewhere (nijboer et al). Both terms can be time-dependent: as the Earth rotates, the ionospheric structures move, telescope patterns (in most cases) rotate with respect to the sky and telescope pointing varies with time. Here we focus on dealing with the effects due to the primary beam response of the individual telescopes.

The effective rotation of the telescope beam on the sky for alt-az telescopes, together with varying pointing errors are likely to be the dominant time-varying direction-dependent effects and are expected to be the limiting factor in allowing instruments such as e-MERLIN and EVLA to reach their thermal noise performance in 'deep fields'. For 25-m telescopes at 1.4 GHz, 'background' sources at the half-power point of the beam are typically > 10 mJy, and hence to achieve 1 μ Jy rms noise over the central part of the field, such source need to be subtracted with a dynamic range of $>10,000:1$. A pointing error of 30arcsec on one telescope would cause a differential direction dependent error of order 0.01. Depending on how well the pointing models have been established and determined, pointing errors could be significantly larger than this. Accurate correction for direction-dependent effects is also important at mm wavelengths, where it is often necessary to make mosaics of complex targets which are much larger than the primary beam.

In several arrays, especially e-MERLIN and EVN, but also ALMA, baselines are formed between telescopes which have quite different primary beam responses. The EVN consists of a network of telescopes which are almost all different, and range in size from 20m to 100m, with different optics and structures. e-MERLIN also includes quite different telescopes, with different diameters and optical arrangements and ALMA will in future wish to form baselines between antennas in the main array (12-m antennas) and the compact array (7-m antennas). Even for notionally identical telescopes, the beam patterns can differ from an idealised, parameterized model, due to the way the telescope is set up or limitations in the electro-magnetic modelling of such structures. Ultimately, it may be necessary to use a combination of the modelled and empirical complex voltage patterns of individual antennas to understand, simulate and correct for direction dependent effects. The work reported here uses both approaches. In the first part, model voltage patterns derived for the ALMA antennas by EM simulation and ray-tracing are compared with measurements on the sky. The second part is concerned with a series of detailed measurements of the complex voltage patterns of the telescopes which make up e-MERLIN, and providing these in a way which can be

used by the Voltage Pattern Manager, developed for CASA as part of the ALBiUS deliverable 6.2.3 by Dirk Petry at ESO. Additional work has been done on generalised considerations for primary beam issues for wide-field mapping by STG, RJB, NW, AMSR, TWBM.

The remainder of this section outlines the algorithms proposed for the correction of direction-dependent effects and the methods by which antenna voltage patterns are typically derived for cm and mm-wave antennas. Two a priori techniques, ray tracing and electromagnetic simulation, are described in more detail in Section 3. The primary beam corrections derived by these methods for the ALMA 12m antennas are tested against measured data in Section 4, where we demonstrate that they give much better results than earlier approximate estimates. Section 5 outlines the measurement of e-MERLIN antenna voltage patterns using holography on astronomical sources and Section 6 shows initial results from this technique.

1.2 Direction Dependent Calibration Algorithms

The measurement equation which relates the effects of the instrumental response (telescopes and atmosphere) and the sky image $I(\mathbf{s})$ to the observed visibilities V_{ij} on the baseline b_{ij} between telescopes i, j can be written as

$$V_{ij} = M_{ij} \int M_{ij}^S(\mathbf{s}) I(\mathbf{s}) e^{2\pi i \mathbf{s} \cdot \mathbf{b}_{ij}} d\mathbf{s}$$

where M and M^S are the direction-independent and direction-dependent Mueller matrices which represent the instrumental response. The Mueller matrix is the outer product of the two telescope-based Jones matrices:

$$M_{ij}^S = J_i^S \otimes J_j^{*S}$$

$$J_i^S = \begin{bmatrix} J_i^p & -J_i^{pq} \\ J_i^{qp} & J_i^q \end{bmatrix}$$

Where p and q refer to the two polarization states/channels for each telescope. The cross polarized terms pq correspond to polarization leakage effects and are not the primary concern here, although they are of course important for polarization imaging and will be important at high dynamic range even for total intensity imaging. The telescope voltage patterns for the parallel polarizations are then J^p and J^q .

Iterative reconstruction of the best model from the data in general involves a forward step, in which the model visibilities are calculated from the existing model image and the measurement and a backward step where the residual visibilities are propagated backwards to the image plane. The forward step requires high accuracy but the iterative approach allows the backward step to be approximate, and may typically use the gridded data for the Fourier transform to the image plane. The accurate forward step requires accurate knowledge of the telescope Jones matrices and hence ideally would use an accurately measured telescope voltage beam for each of the two telescopes on each baseline. So far, all the work on correcting for primary beam effects has been done using parameterised models of the primary beam (eg as implemented in the AIPS package for the VLA and other arrays), simple Airy disks (used in CASA) or results from EM simulations for perfectly aligned telescopes.

Bhatnagar et al (2008, AA 487, 419; 2012) have described a deconvolution approach as follows:

1. Initialise the source (sky) model using any prior knowledge
2. Compute the residual visibilities using the telescope beam patterns
3. Compute the residual image using a convolving function in the gridding step based on the Fourier transform of the Mueller matrix
4. Update the model image in a minor cycle, as in CLEAN
5. Go to 2 until acceptable convergence

This approach is based on the w-projection algorithm (Cornwell et al 2008), and is known as A-projection. Nijboer have described an implementation of this approach, primarily targeted at LOFAR for sub-task 6.2.5

Unfortunately, the A-projection algorithm is not yet available in the released version of CASA, so the original aims of the deliverable could not be achieved. However, significant software infrastructure development was carried out at ESO (RL, DP) in support of this effort. In particular, as part of the ALBiUS work, the ALMAAperture class for using the antenna response patterns to correct for direction dependent effects in imaging in heterogeneous arrays was further designed and implemented, in collaboration with S. Bhatnagar (NRAO). It was realised that a lot of investigation would be required to derive and cross-check sufficiently accurate voltage patterns. This became the main aim of deliverable 6.2.2 and is described in detail in the current report.

1.3 Methods of determining voltage patterns (RL, DP)

The important case for higher frequency arrays such as e-MERLIN and ALMA is that of a known antenna voltage pattern which is significantly more complicated than the simple, axisymmetric approximations used to date. This is the case of a fairly directive antenna at frequencies sufficiently high that ionospheric anisoplanatism is not a serious problem.

A number of different methods can be used to quantify the antenna voltage patterns:

1. Empirical models of the primary beam (eg polynomials)
2. More elaborate parameterization based on Airy disk
3. Geometrical optics approach from ray-tracing, which allows the incorporation of non-axisymmetric effects and measured optical aberrations
4. A priori electromagnetic simulations, which include the effects of antenna receiver optics and other passive components (made for the ALMA antennas)
5. Measurements of antenna voltage patterns by scanning/astronomical holography

The infrastructure for incorporating these voltage patterns into CASA was a separate ALBiUS deliverable (6.2.3). This is described in detail elsewhere, but to be self-contained we give a summary here.

In AIPS and also in CASA before release 3.2, all default primary beams in CASA were provided only as analytical functions (1 and 2 above). Primary beams in the form of images were not supported. In order to make simulated primary beam images easily available to the CASA user, a unified general access scheme (on the C++ level) to interferometer antenna responses patterns in CASA (the

AntennaResponses table) was designed and implemented. This has been an integral part of CASA since release 3.2 and is well accepted.

Furthermore, on the user interface level, the “vpmanager” (Voltage Pattern Manager) part of CASA was refactored and enabled to use the AntennaResponses tables. The new vpmanager is part of release 3.4.

2. A priori voltage patterns

The two principal techniques by which accurate voltage patterns can be derived for realistic antenna models (including the effects of central blockage, feed support legs and deviations from axisymmetry) are ray tracing and full electromagnetic simulation (methods 3 and 4 of Section 1.3). The former is, of course, much simpler and faster but applies only in the geometric optics limit. It is a reasonable approximation at mm wavelengths for the types of antennas typically used in radio astronomy, but does not describe the receiver components (e.g. the feed horn) very accurately. Deviations from optimum alignment or surface accuracy can easily be incorporated. The latter is expensive to compute, but should give very accurate results provided that the antenna and receiver system are set up and aligned exactly as assumed. Adding in the effects of errors requires a full re-computation of the voltage pattern. The two methods are described in Sections 2.1 and 2.2, below.

2.1 Ray tracing

A method of deriving antenna response patterns using ray tracing in the geometric optics approximation was developed for VLA and EVLA antennas by W. Brisken (CASSBEAM Software for Cassegrain antenna modelling, NRAO).

Ray tracing is used to determine the electric field at each grid point on the aperture plane. This is done through a complicated process that will be discussed briefly here.

The approach is to calculate the electric field on a uniformly spaced grid on the aperture plane. Since the ray may not travel along \hat{z} from the primary to the aperture plane, some iteration is required. First the (x, y) position of the grid point to be calculated is taken as the starting point on the primary. The corresponding z value and the surface normal are then calculated for that point on the primary. The virtual ray is then reflected off the subreflector.

It should be noted here that nowhere is the subreflector ever stored as a rastered surface -- it is recomputed each time it is needed, and this is likely far more efficient than searching a tabulated surface for an intersection point. The subreflector displacement and rotation are then considered. A ray is then projected from the feed to this point on the subreflector. The process is reversed now that a guess for the appropriate subreflector point is made. A ray is traced from the feed to this point on the subreflector, reflected toward the primary, and finally reflected to the aperture plane. The (x, y) value of the intersection of the ray with the aperture plane is compared with the initial (x, y) .

An offset is applied to the original value and the iteration continues. About 3 iterations are sufficient for convergence, although about 7 are done in practice.

Once points on both the aperture plane and the primary are known, the final ray is defined. Three rays are shot out from a small triangular region of the aperture plane and are used to calculate dP/dA , the flux through the point of interest on the aperture plane. This value includes the taper of the feed, the dilution of the beam due to expansion, and the effects of all the surface shapings. The

length of the ray is then used to derive the phase of the field on the aperture. Finally, the two circular polarization vectors are propagated from the feed. Reflections obey the proper boundary conditions for a conducting surface:

$$E_{\parallel} = 0$$

$$E_{\perp} = 0$$

The electric field, decomposed into a linear polarization basis for each outgoing circular polarization, is computed on the aperture plane grid.

The code includes a general description of a Cassegrain-like reflector with a central hole, four feed support legs (geometrical blockage only) and an offset feed. It can therefore give a reasonable description of ALMA or EVLA antennas, including the important beam squint effect in the latter case. It has the great advantage that it can be computed on-the-fly and it is therefore very straightforward to account for rotation of the beam pattern on the sky (parallactic angle). It actually provides a better approximation in the ALMA case (shorter wavelengths) than for EVLA, since the unmodelled effects of diffraction are significantly less.

When it became clear in late 2010 that detailed simulated primary beam models would initially be available for a subset of the ALMA frequency bands (3,4,6,7, and 9) and also only for the 12 m, not the 7 m antennas, an additional way of response simulation was sought for and found in this ray-tracing code.

The code by W. Brisken had previously been pasted into CASA in a non-object-oriented way and parameters were hard-wired. In order to enable the sharing of the code between EVLA and ALMA analysis routines and to permit setting of the parameters without recompiling CASA, the first step was to extend the previously developed unified access scheme ("AntennaResponses") to permit the setting of the parameters through user-modifiable text files. Default versions of these parameter files are distributed with CASA.

The EVLA parameters were then translated into this new representation and the code was extensively tested with EVLA data.

The ALMA parameters were derived from the technical documentation of the four antenna types (the three 12 m types and the one 7 m type) and also entered into the new parameter files. The resulting voltage patterns were checked against those from EM simulations (see below), which were used to tune the assumed illumination pattern.

Furthermore, measurements on real ALMA antennas had indicated that astigmatism was possibly an important additional parameter to include in the simulations, so the ray tracing code was extended to permit the introduction of astigmatism via the coefficients of the canonical Zernike polynomials which the user can control. This approach could be extended to more complex models involving multiple Zernike modes as used, for example, in modelling of the variation with temperature of the ALMA antenna surfaces.

Finally, the ray tracing code was cast into a proper class with a singleton interface to the rest of the code.

A comparison between parallel-hand voltage patterns for an ALMA antenna at a frequency of 100 GHz computed by EM simulation and by tracing is shown in Fig. 1. While the sidelobe patterns predicted by ray tracing at large angles from the field centre are inevitably inaccurate, the two beam patterns are very similar out to the first null.

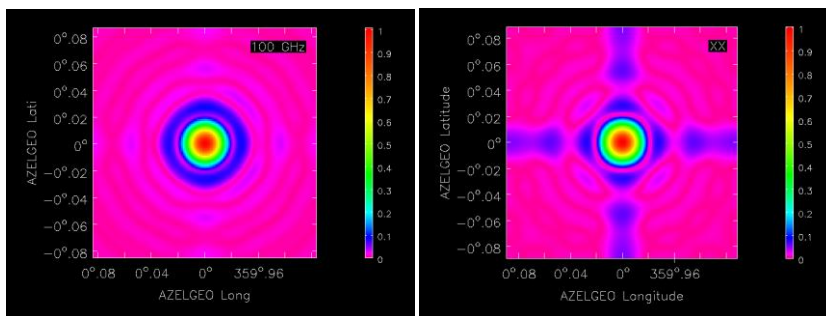


Fig1: ALMA antenna voltage patterns at 100 GHz: EM Simulation (left) and Ray Trace (right)

2.2 EM Simulations

The electromagnetic simulations of the ALMA antennas used in this work are described in Pontoppidan (2007) (Pontoppidan, K, 2007, Electromagnetic properties and optical analysis of the ALMA antennas and Front Ends, TICRA, Copenhagen). They include support leg blockage effects, detailed reflector geometry, surface deformations and front-end analyses. They were computed using GRASP, an antenna modelling program, developed by TICRA, which uses physical optics and the physical theory of diffraction to compute radiation patterns. The PO calculations are carried out by computing induced currents on optical surfaces, which can then be used to compute radiation patterns. This works well for smooth surfaces, but breaks down near edges and for small structures, which are treated with PTD.

The ALMA antennas are designed as conventional, rotational symmetric Cassegrain reflector antennas. The main reflector is a paraboloid with a diameter of 12 m and a focal length of 4.8 m. The subreflector is a hyperboloid with diameter of 0.75 m and a magnification of 20. These

four parameters are sufficient to define the antenna system. The antennas are designed to operate in 10 frequency bands from 30 to 950 GHz, using separate receivers in a single cryostat. A special front-end design has been carried out for each frequency band in order to generate a Gaussian Beam with a given waist diameter, location and orientation. The beams are tilted in the plane

containing the antenna. One significant complication is that it is intended to displace and tilt the subreflector to maximise the gain for the receiver band in use.

Although the basic optical parameters of the three designs of 12m antenna used in the ALMA array are identical, there are differences of detail, particularly in the design and location of the feed support legs, which are at different orientations in one of the designs (AEM) compared with the other two (Vertex and Melco). The following effects have to be modelled: (a) illumination of the struts by the reflected field from the main reflector; (b) shadowing and changes of the main reflector currents caused by direct feed illumination of the struts and (c) reflection in the main reflector of the scattered field from the struts, where the incident field on the strut comes from the main reflector. The components of the receiver optics (mirrors, lenses, polarizing grids, corrugated feed horns) for each frequency band are also included in the analysis. Responses have been calculated at a number of representative frequencies within each observing band; in practice for wide-band imaging, the response closest in frequency will be scaled to the observing frequency (errors from this approximation are very small compared with deviations between as-built and ideal optics).

We concentrate on the observing bands currently in use for observing at ALMA: Band 3 (84-116 GHz), Band 6 (211-275 GHz), Band 7 (275-373 GHz) and Band 9 (602-720 GHz).

Python code was developed to read all TICRA simulations and convert them into the required representation in CASA image format. Several iterations with one of the imaging developers at Socorro (K. Golap) were performed to agree on the final image format which is a four-plane (in the Stokes dimension) complex-valued image containing the voltage pattern for the parallel hands in a linear basis (XX and YY) and the cross-hands (XY and YX). The directional coordinate system is of type AZELGEO centered on (0.,0.). The reference frequency of the responses is stored by creating a degenerate spectral axis centered on that frequency. An alternative format representing the complex electric field pattern was developed in parallel.

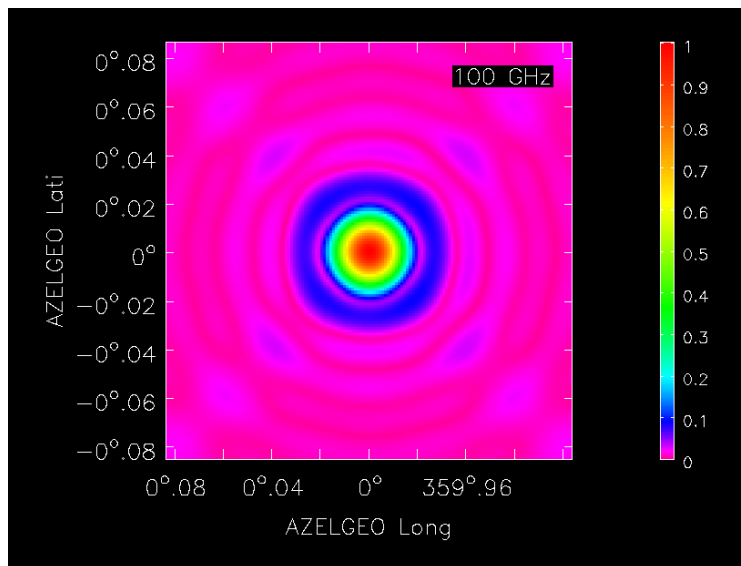


Fig 2: EM Simulation: ALMA 100 GHz, AEM antenna type

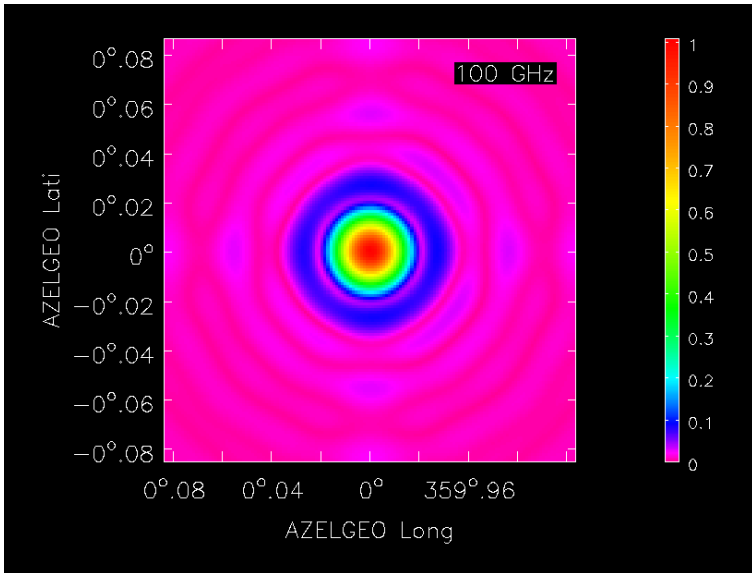


Fig 3: EM Simulation: ALMA 100 GHz, Vertex antenna type (note the 45 deg rotation in the support leg structure)

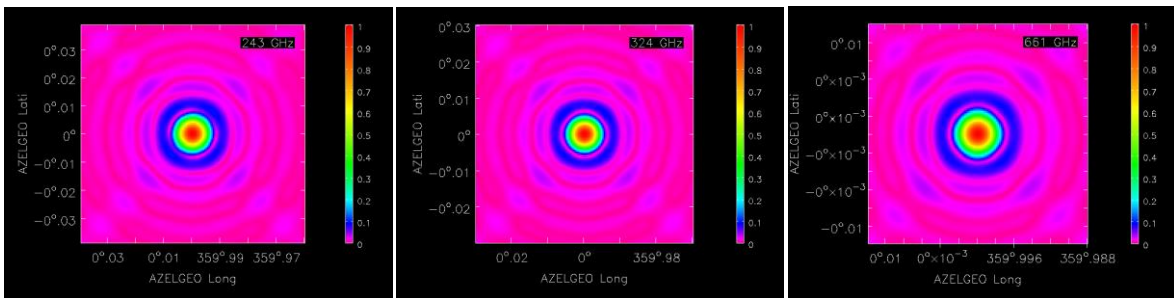


Fig 4: EM Simulation ALMA 243, 324, 661 GHz, AEM antenna type

Note that preliminary EM simulations for EVLA using GRASP have been described by Brisken (EVLA Memo 58). It would be possible to develop these further, and to carry out additional simulations for the previously unmodelled ALMA antennas and bands, e-MERLIN and EVN.

3. Imaging Tests with ALMA

In order to perform an initial validation of the computed ALMA antenna voltage patterns, tests were carried out to measure the azimuthally averaged primary beam response (i.e. the radial variation of the power pattern). At the time of these tests, the array had mostly one variety of antenna (the Vertex 12m design). Several sets of ALMA data were obtained, as described below.

Several sets of ALMA data were obtained to assess the validity of the ALMA primary beam correction.

3.1 Observation of an 11-point mosaic with 12 antennas

A band 3 observation of a 11 pointing hexagonal mosaic with a bright quasar at various positions in the field was carried out with 12 ALMA antennas in May 2011. This dataset was first analysed with CASA 3.2 and immediately demonstrated that the multiplicative primary beam correction implemented in this release (based on an analytical Airy disk approximation) was completely inadequate.

Fig5 shows the mosaic without primary beam correction and Fig.6 the effect of implementing the default correction. A scaling by a factor of 1.12 improved the correction at large radii (Fig 7)

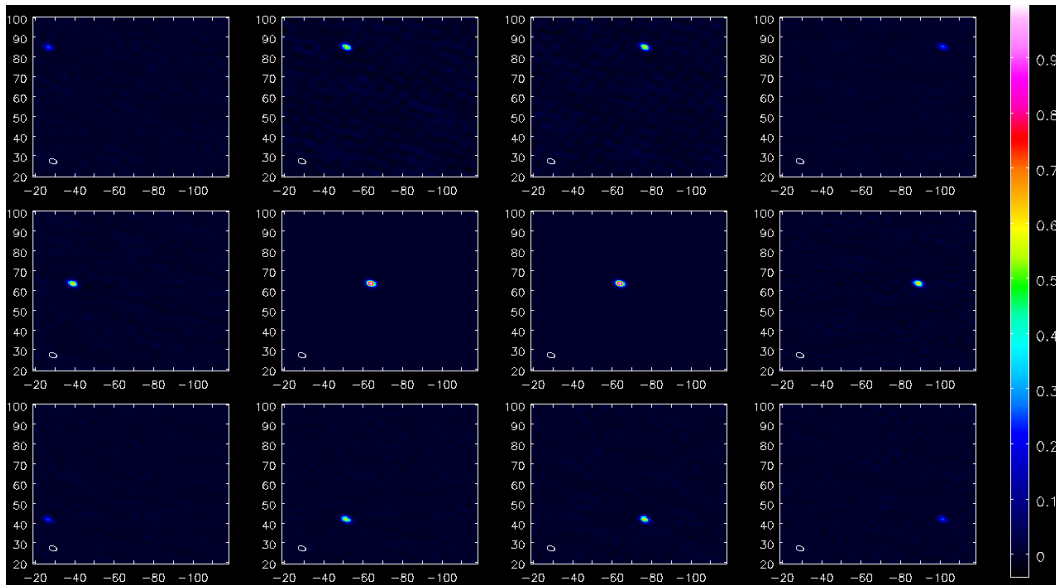


Fig 5 Results from ALMA test dataset 1 showing the images of the observed quasar without any primary beam correction. The object, which should be of the same brightness in all images in the absence of primary beam effects, is much fainter the farther it is away from the field centre.

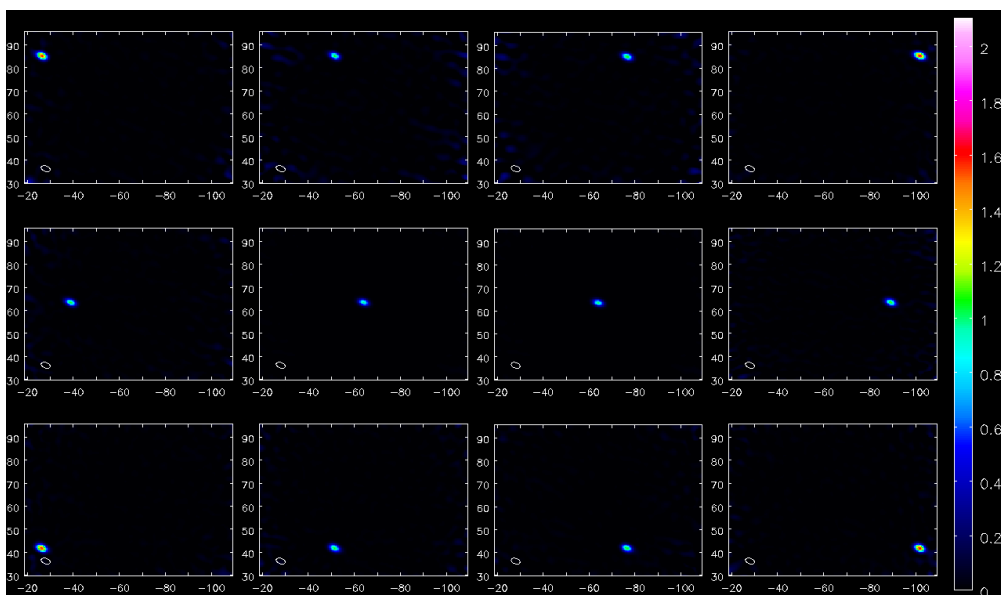


Fig 6: As Fig 5 but with the standard CASA 3.2 ALMA primary beam correction applied. It is clear that the off-axis images are too bright..

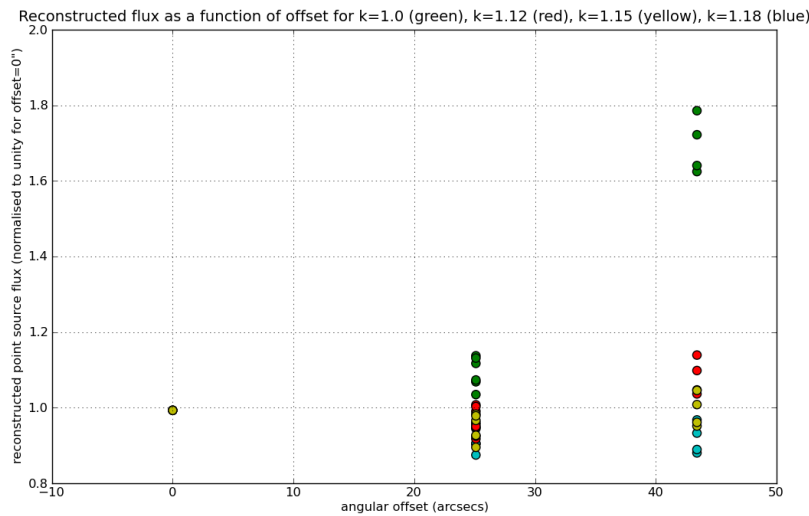


Fig 7: Attempt to improve the analytical (Airy-disk) based primary beam model in CASA 3.2 by scaling it (factor k). Green: the points derived from Figure 6, i.e. using the standard ALMA response used in CASA 3.2 and 3.3. An overcorrection by up to 80% (!) is visible at ~45 arcsec angular offset and up to 16% at 25 arcsec angular offset. Red, yellow, and blue: effect of setting the response scaling factor k successively to 1.12, 1.15 and 1.18 (1.12 was used in release 3.4).

Fig 8 demonstrates the improvement achieved in this first simple test by using the a priori primary beam response derived azimuthal averaging of the EM simulations without further tuning.

The blue points for both the 25 arcsec and the 43 arcsec angular offset are evenly distributed within less than 8% deviation around 1.0, the ideal value. The remaining scatter is at least partially due to the large range of elevations (55 deg to 85 deg) over which this data set was acquired without system temperature corrections.

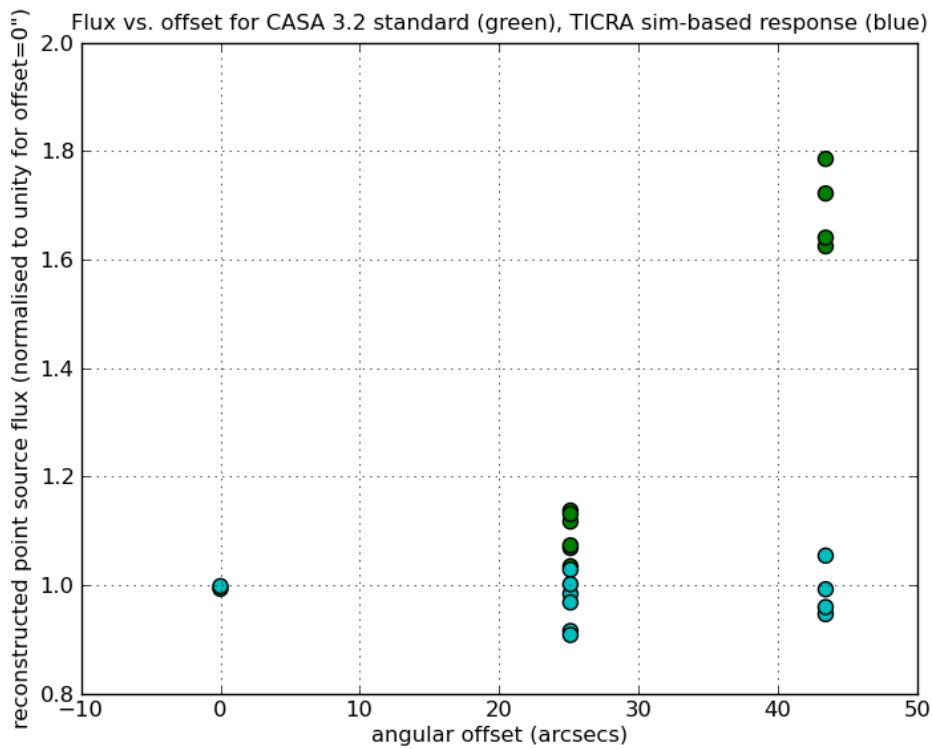


Fig 8 Improvement of the primary beam correction from using the simulated ALMA responses developed in this work (based on the TICRA) simulations (blue points) compared with the standard ALMA primary beam correction in CASA 3.2/3.3 (green points).

3.2 Observation of a 61-point mosaic with 19 antennas

As a second more detailed test, a hexagonal mosaic of 61 pointings was observed with ALMA with 19 antennas (all except two were of type Vertex) in January 2012. This dataset was again first analysed with the standard CASA 3.3 procedure with primary beam correction. The results are shown in Figures 9 and 10.

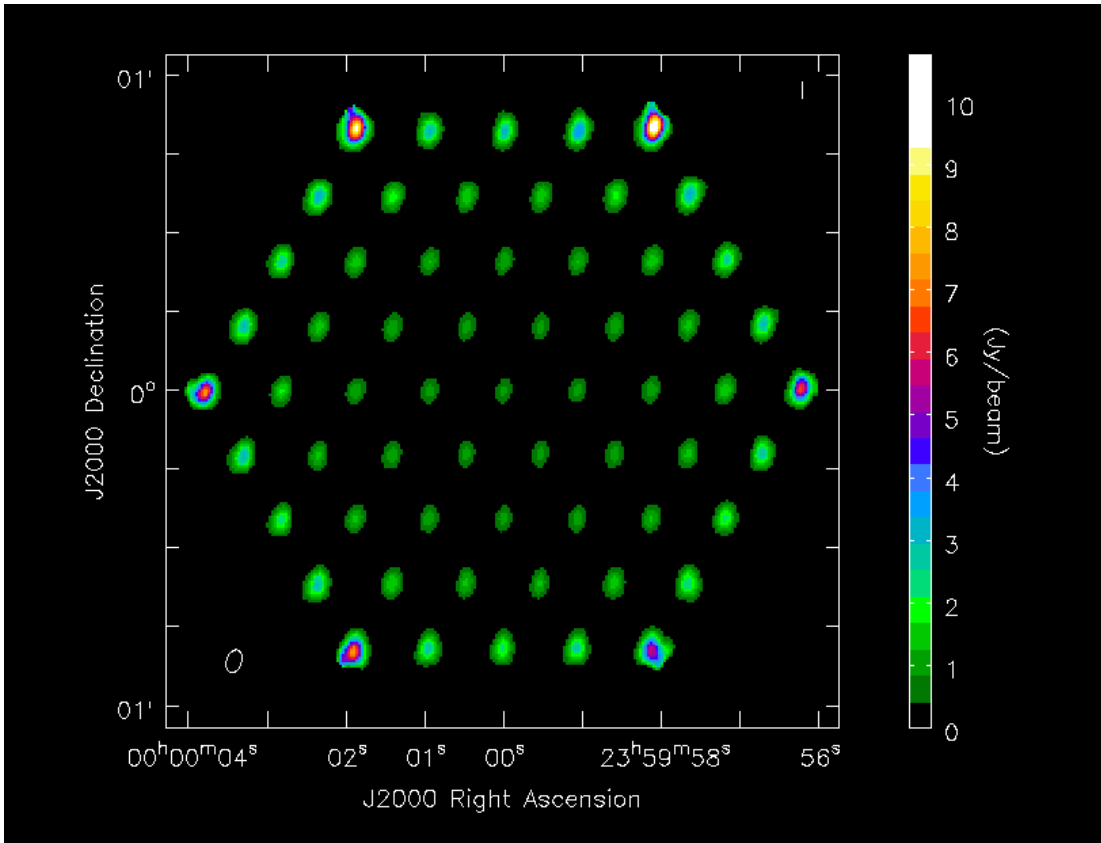


Fig 9 Results from the standard analysis of test dataset 2 (subset taken at 99.9 GHz) with CASA 3.3. The reconstructed flux is strongly dependent on the offset from the primary beam centre.

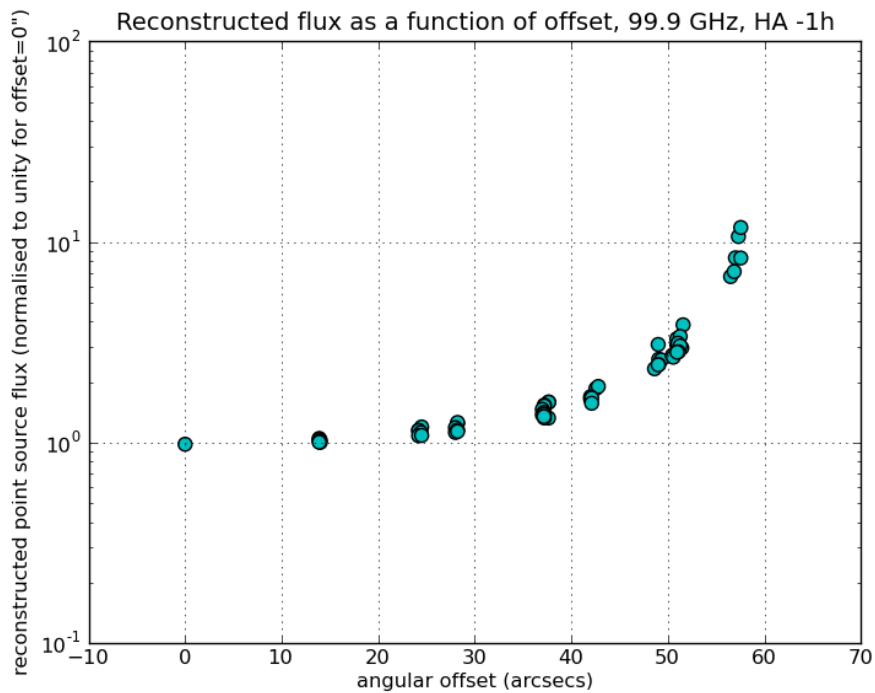


Fig 10: The measurements shown in Fig 9 plotted vs. angular distance from the center of the field of view

Both Figs 9 and 10 demonstrate the inadequate state of the primary beam response correction for ALMA in CASA 3.2 and 3.3. Since the data quality is higher than in the test dataset taken in 2011, the scatter of the points is reduced and a smooth trend in the deviation from the ideal value 1.0 is clearly visible in Figure 10. The overcorrection is increasing faster than linearly with angular distance and reaches almost a factor 10 at an angular distance of 57 arcsec (= 2 times the nominal ALMA primary beam radius at ~ 100 GHz). Very similar plots were obtained from the three other frequency ranges observed (98.9 GHz, 109.2 GHz, and 111.0 GHz).

For comparison, the results obtained with no primary beam correction at all are shown in Figures 11 and 12. In particular Fig 12 is instructive because it effectively traces the shape of the primary beam. Furthermore, the intrinsic scatter of the datapoints becomes apparent.

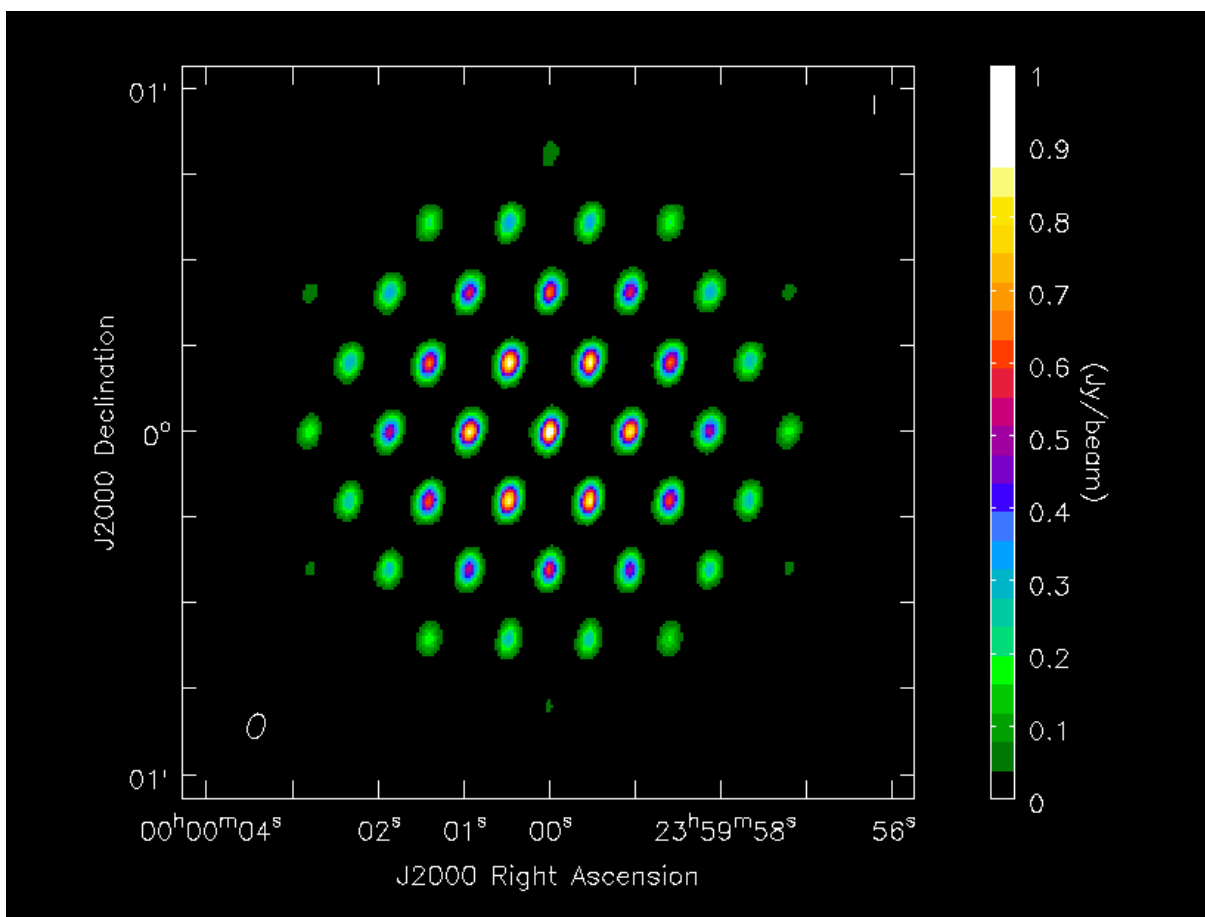


Fig 11 Results obtained with no primary beam correction from the 61 pointing dataset.

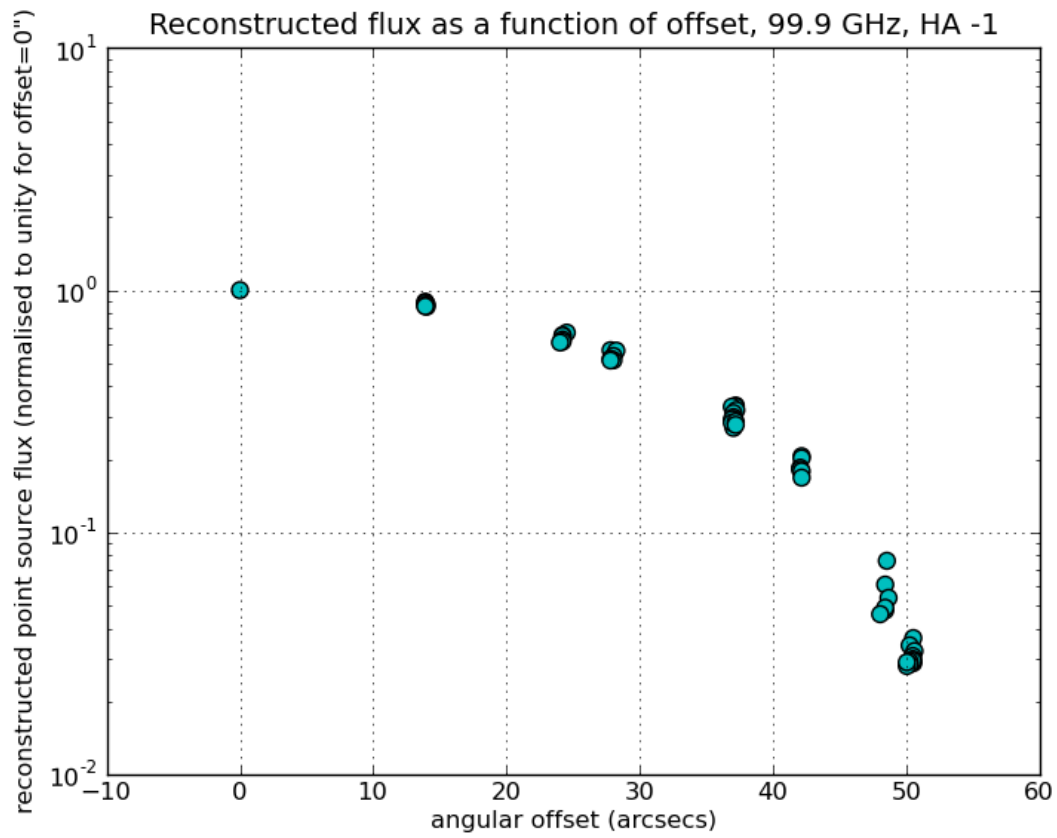


Fig 12: Fluxes obtained from the results in figure 11 (no primary beam correction) plotted against angular offset from the centre of the beam

As discussed in the previous section, the analytic ALMA primary beam description was tuned in CASA 3.4 to match the results obtained with dataset 1. With this improvement, the results in Figs 13 and 14 were obtained.

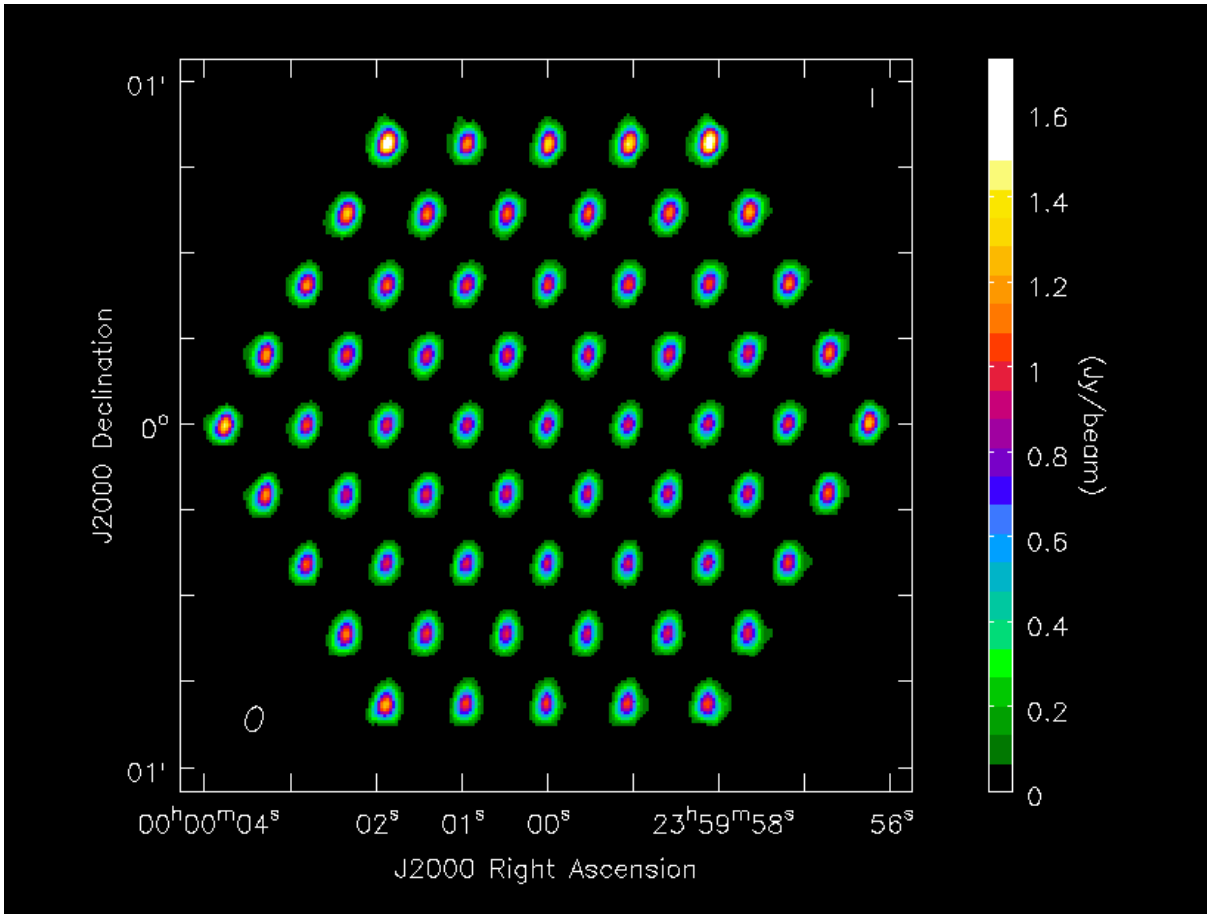


Fig 13 Results obtained from dataset 2 (subdataset at 99.9 GHz) with the default primary beam correction from CASA 3.4 (an Airy disk, scaled using the results from test 1).

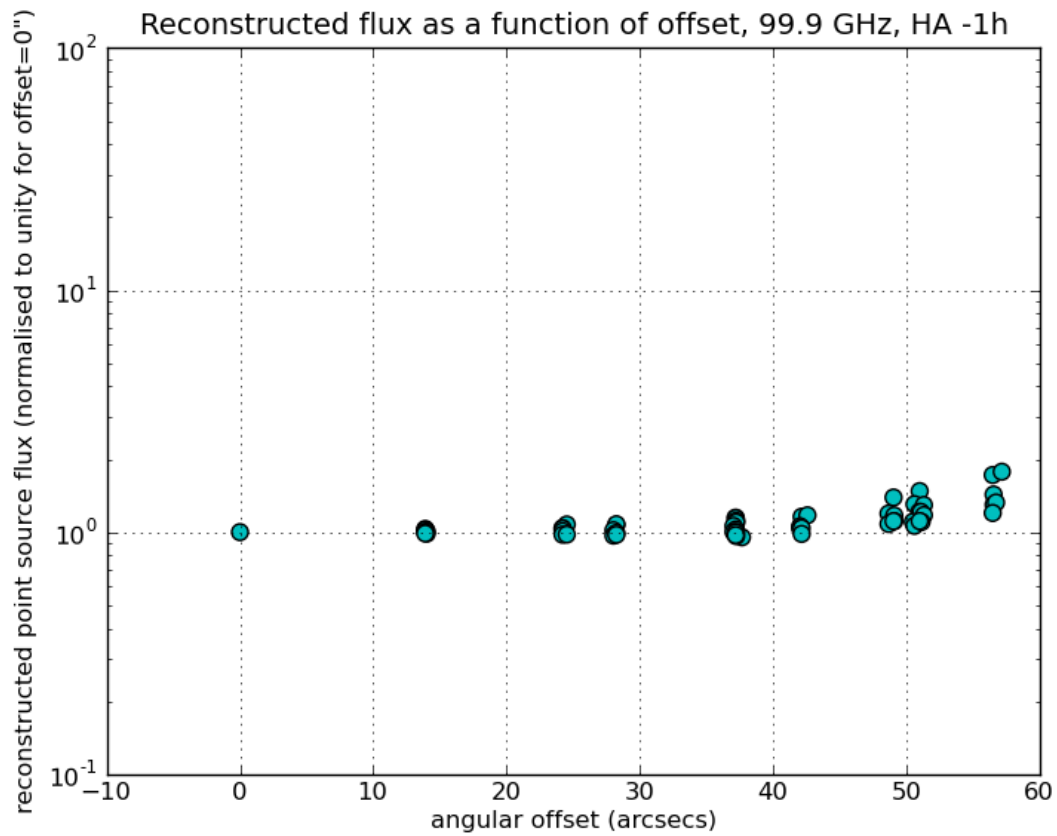


Fig 14: The results from Figure 13 plotted against angular distance from the centre of the primary beam.

As can be seen from the figures, the tuned Airy disk response in CASA 3.4 is a big improvement over the Airy disk used in CASA 3.3. Especially at angular offsets less than the nominal primary beam radius (~ 27 arcsec), the correction is good. Beyond that, however, the beam underestimates the true sensitivity and hence overcorrects the flux by up to a factor 1.7 (1.5 on average) at angular offsets of 57 arcsec.

Finally, the results using the primary beam correction derived from EM simulations are shown in Figs 15 and 16.

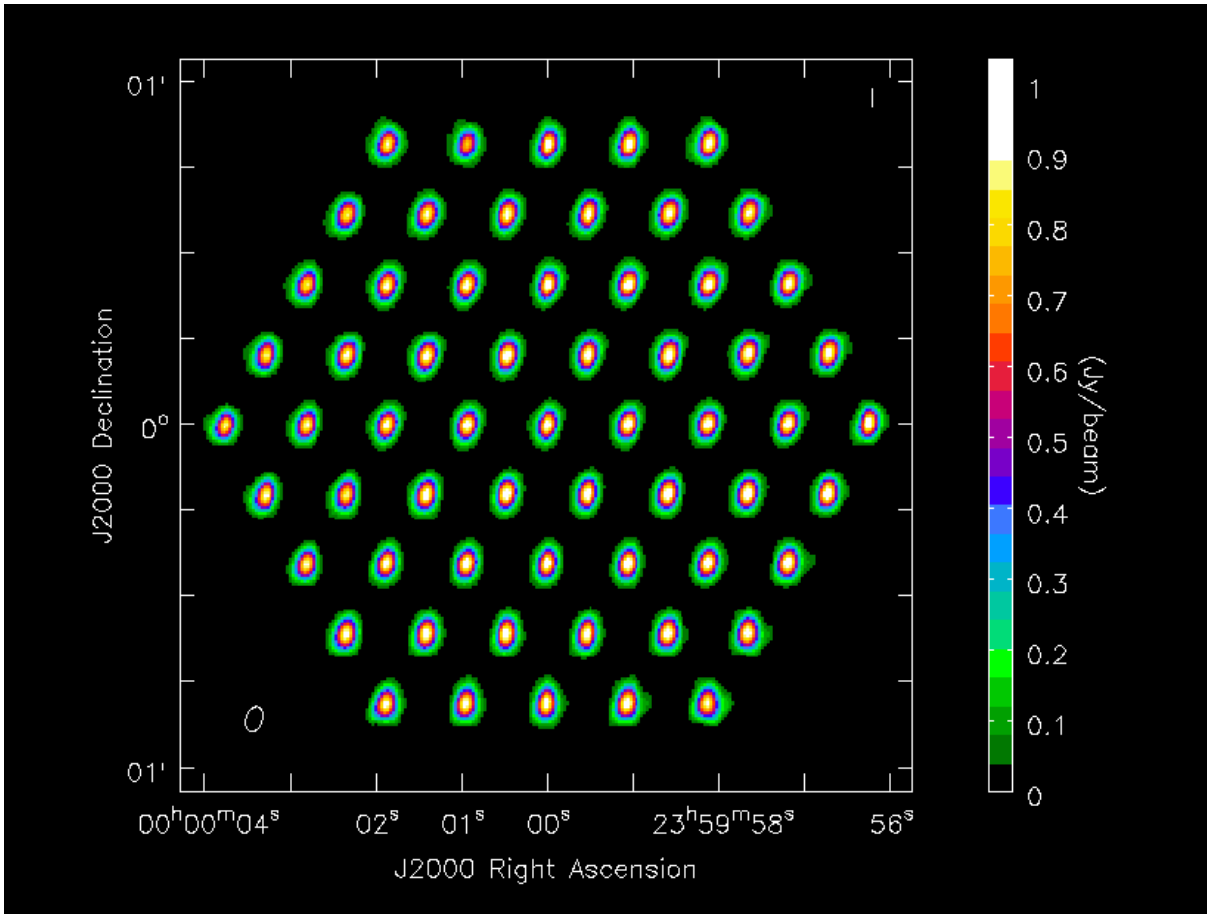


Fig 15:The results from applying the primary beam correction derived from EM simulations to the 61-pointing dataset at 99.9 GHz.

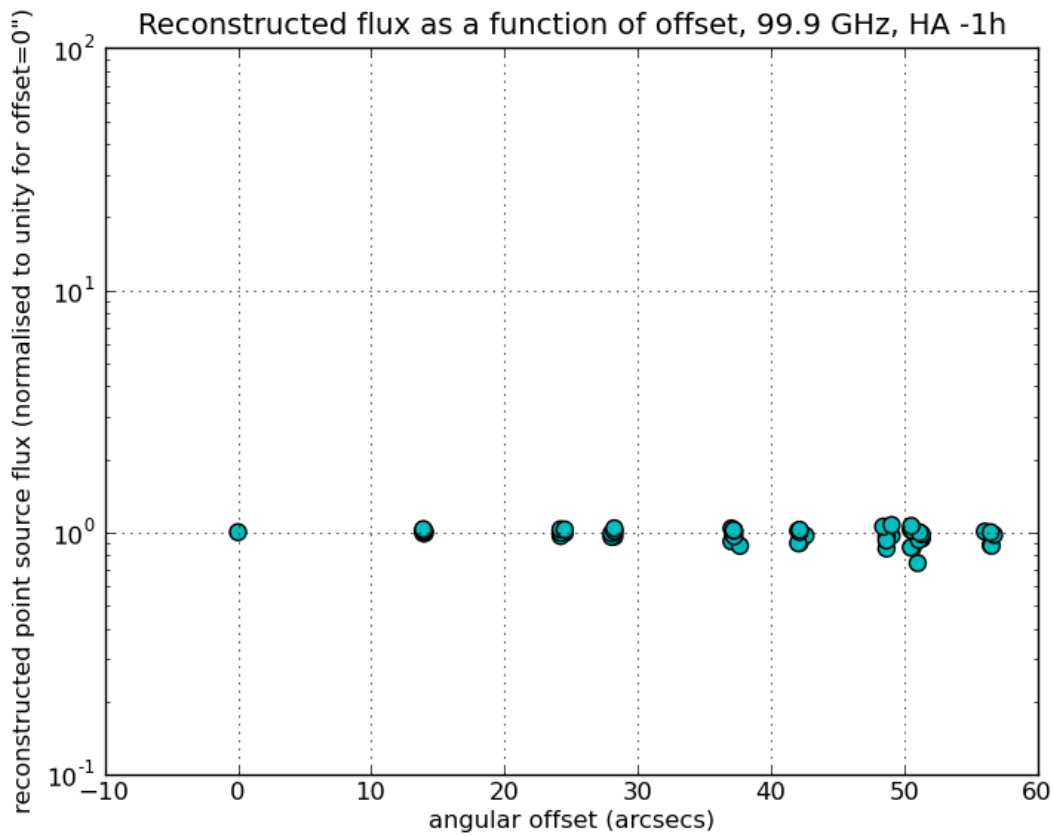


Fig 16: The reconstructed fluxes from the images shown in figure 15 plotted against the angular offset from the centre of the primary beam. The nominal half-power radius is 27 arcsec.

There is a clear improvement over the tuned Airy disk at angular offsets greater than the nominal primary beam radius (~ 27 arcsec). On average the correction is reproducing the flux obtained in the central pointing without any systematic deviations. This confirms that the simulations carried out by TICRA describe the ALMA antenna voltage pattern (in this case the Vertex antenna type) well out to at least two primary beam radii.

In Figure 17, the same points as in Figure 16 are plotted, but on a linear scale in order to show the remaining scatter in more detail. This scatter is mostly caused by noise rather than any systematic error in the correction (the signal to noise ratio of course decreases with increasing angular offset), any residual systematic effect being below 5%.

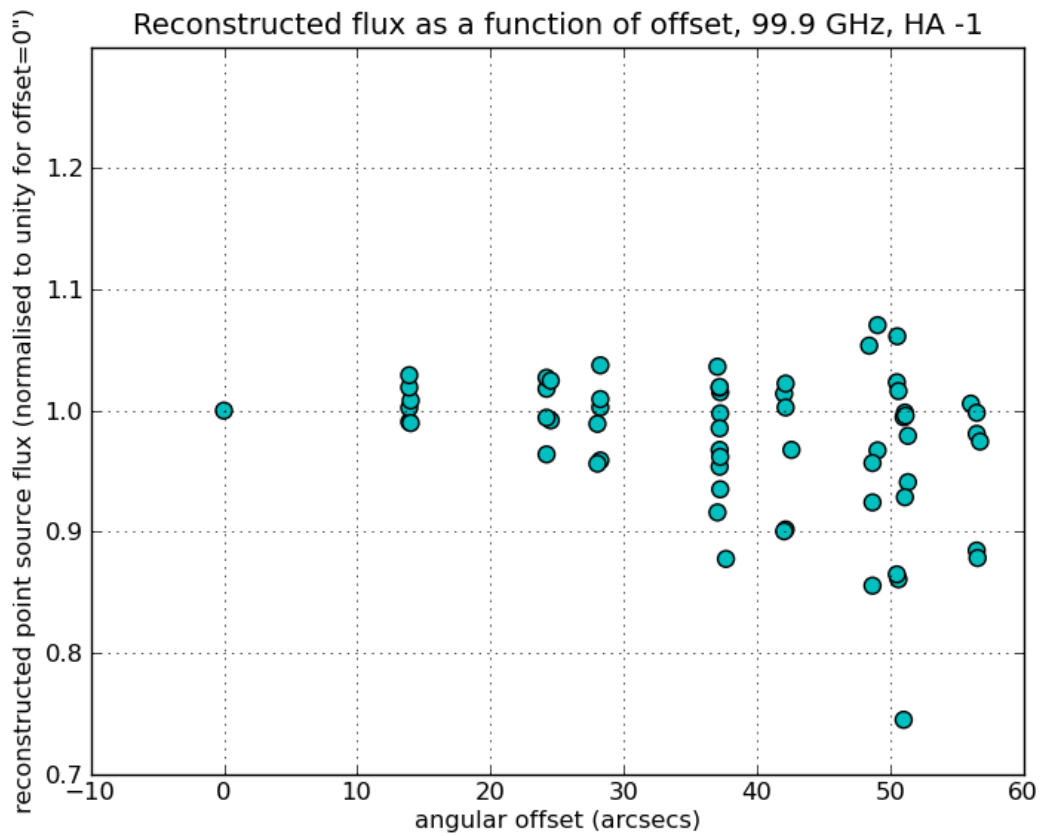


Fig 17: As Fig 16, but plotted with a linear flux-density scale

Finally, we have also tested the ray-tracing code described above. This can also give a very good representation of the primary beam response provided that the taper polynomial, which accounts for the illumination pattern (dependent on receiver optics and therefore not part of the a priori optical model) is tuned to match the half-power radius from the EM simulations. The results are shown in Figs 18 and 19.

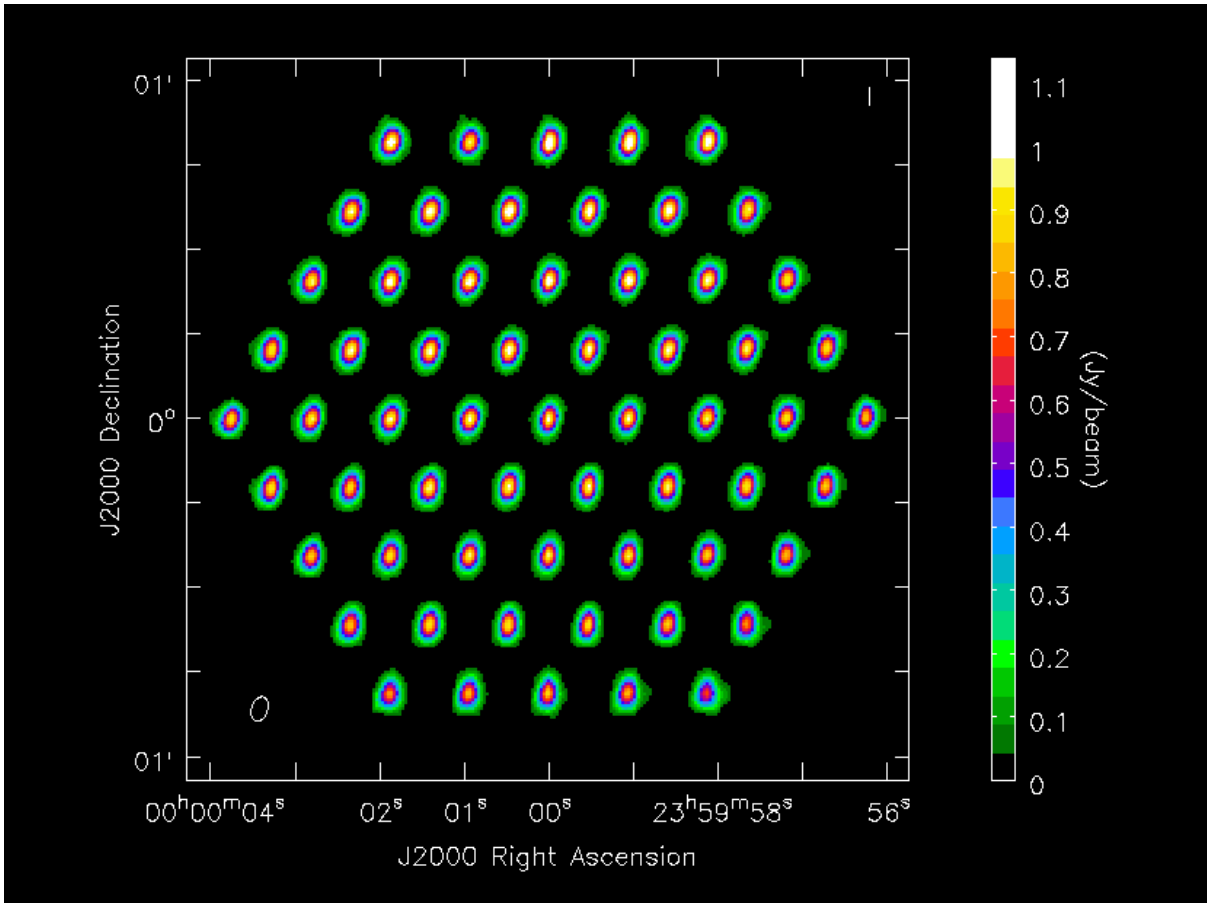


Fig 18: The results from applying the primary beam correction derived from a ray-tracing calculation to the 61-pointing dataset at 99.9 GHz.

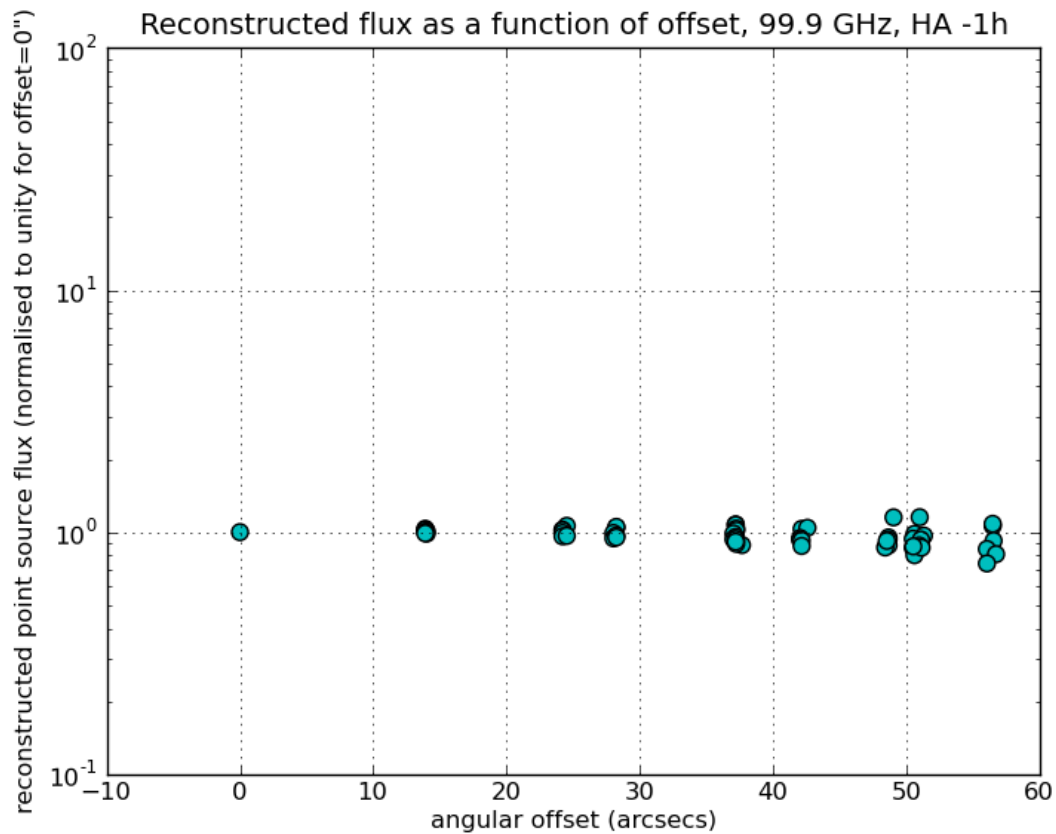


Fig 19: The reconstructed fluxes from the images shown in figure 18 against the angular offset from the centre of the primary beam.

4. Voltage Pattern Measurements for e-MERLIN Antennas

Even if the theoretical antennas and receiver optics can be modelled accurately, structural deformations and other errors may be significant. In this case there is no alternative to accurate measurement of the voltage beam. For heterogeneous arrays of 'legacy' telescopes such as e-MERLIN and EVN, it may indeed be simpler to make empirical measurements rather than embark on a series of simulations of a large number of antenna types. The beams can be determined experimentally by scanning the telescope across a bright source and measuring the response. For an interferometer this process can produce the complex beam pattern by using the complex correlator products and keeping a reference antenna fixed on the source.

Interoperability

Since the CASA package (or at least framework) is the environment where the majority of developments in radio astronomy imaging and calibration techniques are being developed and ultimately implemented, it is important to be able to read data from the new generation of radio interferometers into CASA. For e-MERLIN, a data exporter was written [PAH, RGN, AMSR] to write e-MERLIN data as FITS-IDI files, which could then be read into a CASA Measurement Set using the developed by ESO (RL, DP), with contributions from [PAH, AMSR].

Measurement procedures

During the course of this project the new e-MERLIN system has been commissioned. As well as new receivers, digital back ends, optical fibre transmission systems and a new correlator, all the operational software and data handling has been replaced. As part of this work, new facilities were built in order to set up, measure and analyse telescope voltage patterns.

The measurements are made by scanning one telescope at a time in the array across a bright calibrator source. The scanning pattern can be controlled from the operations GUI and is a raster in azimuth and elevation offset but which uses a go-and return scan in the (continuous) scan direction and includes dwell time at the notional pointing centre between each go-and-return scan. The extra data points at the notional centre are used to calibrate the direction-independent amplitude and phase variations as a function of time. The telescope control systems feed back the pointing errors with respect to the requested scan pattern and these are included in the grid points of the scan data. The complex beam pattern values are the correlated visibilities averaged over each sub-band with a 1-second sampling interval. Each telescope records its pointing position in the main data file every second. The scan rates were relatively slow in order to sample the beam shape in some detail, and with the 1 second integration time it typically took 4 hours of observing to produce a beam pattern which extended out to the second side-lobe for a single telescope.

Figure 20 shows part of such a beam scan observation for the Cambridge telescope as displayed by the e-MERLIN on-line control software. The figure shows the raw correlated amplitudes (in red) and phases (in yellow) with reference to the Pickmere and Darnhall telescopes as a function of time. The gradual cut across the beam can be clearly seen in the amplitudes for the times between the calibration pointings (the horizontal dashed line). It is also apparent from these plots that the raw phases cannot be used without calibration as they are obviously varying with time.

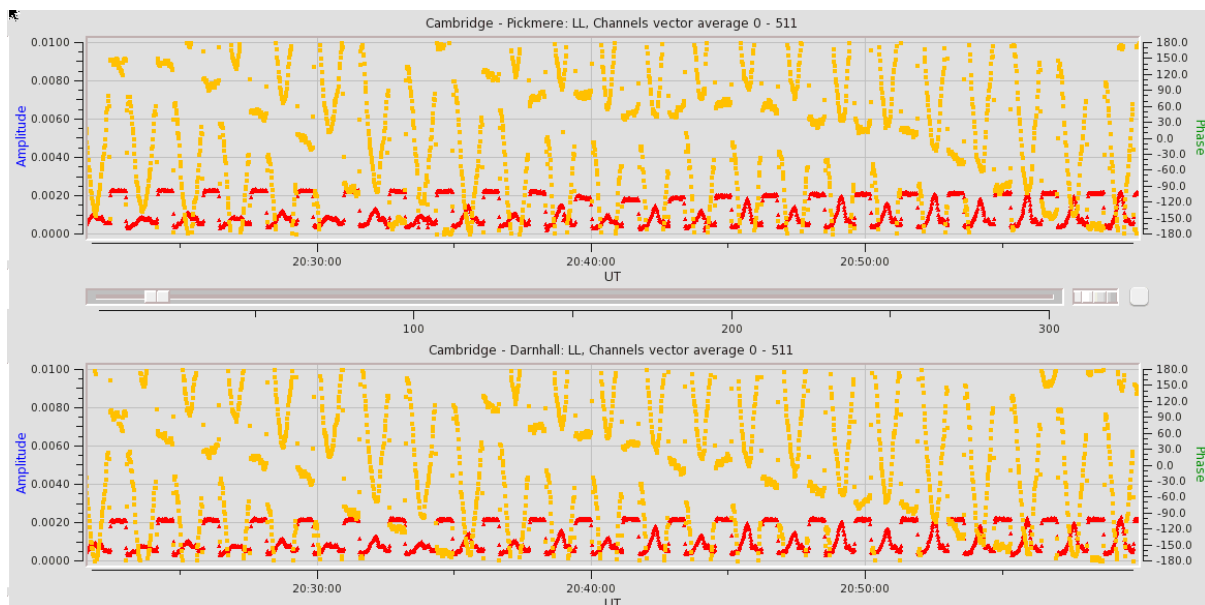


Fig 20: on-line plot showing scanning of one telescope.

In order to calibrate the (direction-independent) delay and phase rate variations the AIPS task FRING is used. Hence the calibration steps were carried out in AIPS, rather than CASA. The data were exported from the e-MERLIN system utilizing the FITS IDI format – The software utility to export into FITS IDI for e-MERLIN was also written as part of the Albius project.

The data processing pipeline for creating the beam patterns was written as a ParselTongue script, as it was necessary to perform data manipulations that are not directly available within standard AIPS. ParselTongue, a previous RadioNet product, provides Python language access to some of the raw data structures within AIPS that enable custom data processing to be done. The first stage of the pipeline is that the time-variable interferometer delays are removed so that the data can be averaged across the sub-band. For measurements at 6 GHz, the sub-band is typically 128 MHz wide, for measurements at 1.5 GHz, 32 or 64 MHz sub-bands will be used.

Next the direction-independent variations in amplitude and phase with time are removed using CALIB on data at the notional pointing centre and interpolating the solutions for the variation over the scanning part of the data.

After the calibration as a function of time it is then necessary to compute the amplitude and phases as a function of the offset position. The telescope pointing offset is recorded in the e-MERLIN data files, but is not exported as part of the FITS-IDI format, so the pointing offsets were extracted as a function of time by a separate utility. These offsets then have to be carefully aligned in time with the calibrated amplitude and phase data and the amplitude and phase extracted as a function of offset.

The following figure is a 3D view of the calibrated data as a function of azimuth and elevation offset from the nominal pointing direction of the Cambridge telescope. The phase (in degrees) of the beam is represented by the colour of each point

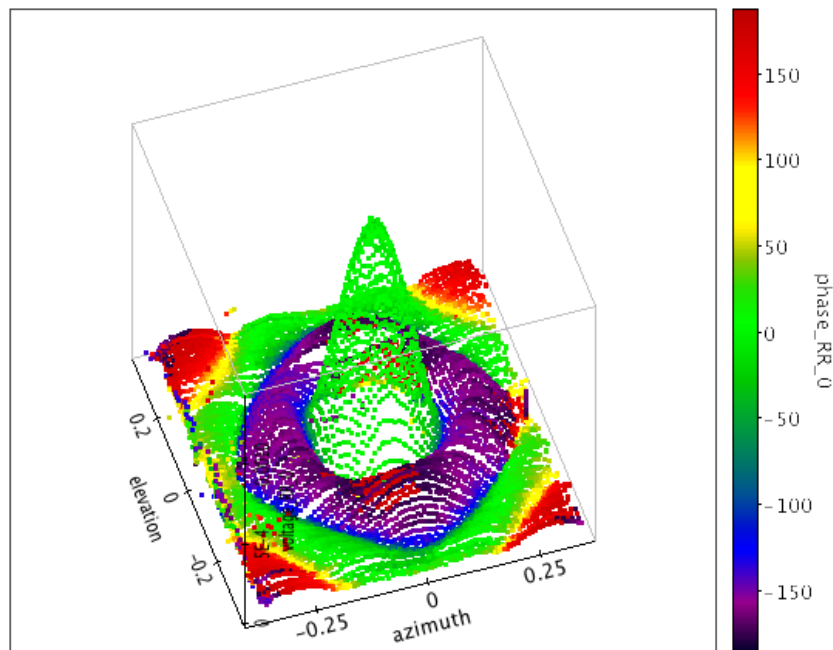


Fig 21: 3D view of the voltage pattern of the Darnhall telescope. Amplitude is shown by the 'height' of the plot and phase is shown by the colour.

The figure was produced using the TOPCAT tool <http://www.star.bris.ac.uk/~mbt/topcat/> which was also used to hand edit any obviously bad points from the dataset, with the 3D view being essential to this process.

5. Measured beams for e-MERLIN antennas

The measured telescope beams display a variety of features and asymmetries that would not be expected from an ideal model of a perfectly configured antenna and feed. In principle, all of the e-MERLIN antennas should have a low order of rotational symmetry (ie a Cassegrain optical system with a quadruped support for the secondary mirror). This would be intrinsic to any analytical or numerical EM model. While every endeavour is taken to ensure that telescopes are optimally set up, in the real world such departures from optimal set up may be comparable to or larger than some of the differences between the different modelling techniques discussed for the ALMA antennas.

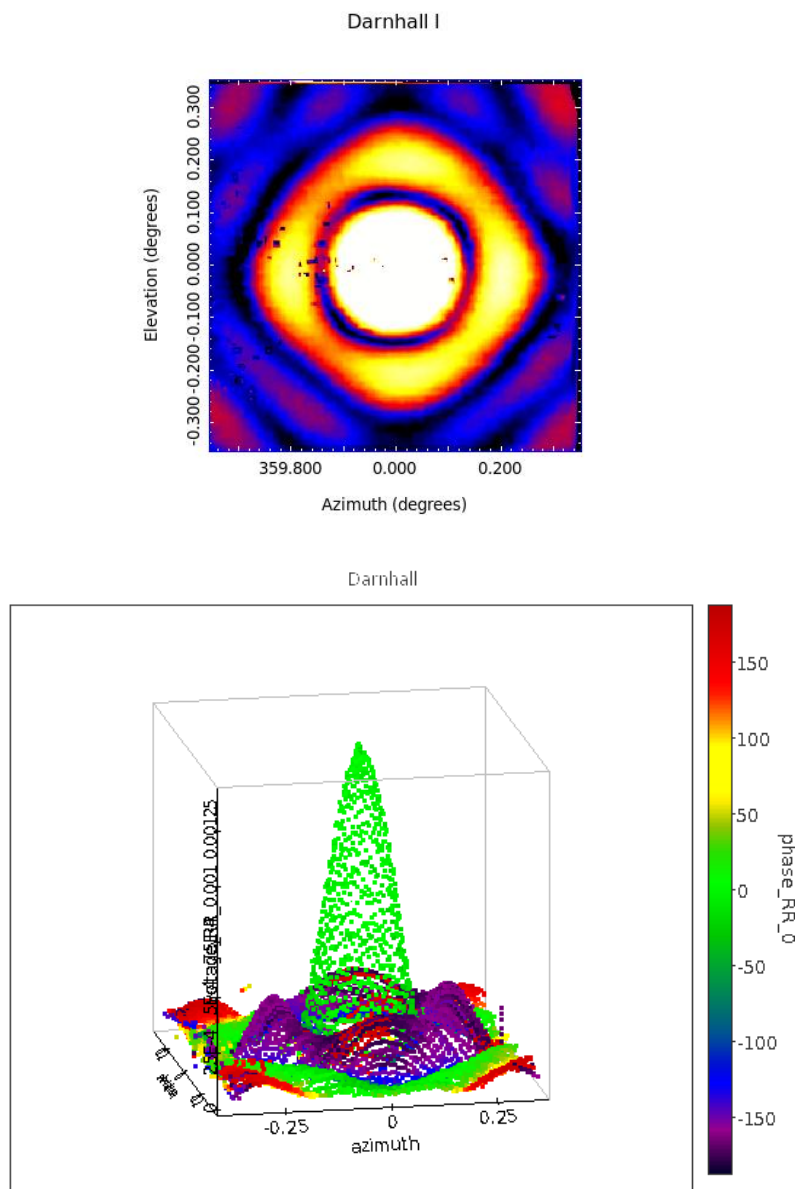
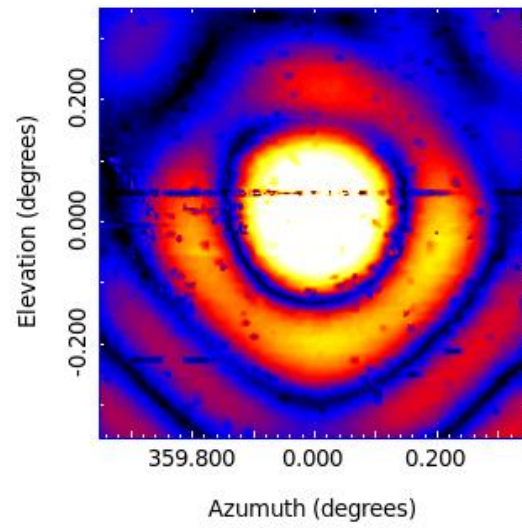


Fig 22: Plots of the Darnhall telescope beam – the expected symmetry can be clearly seen

Pickmere I



Pickmere

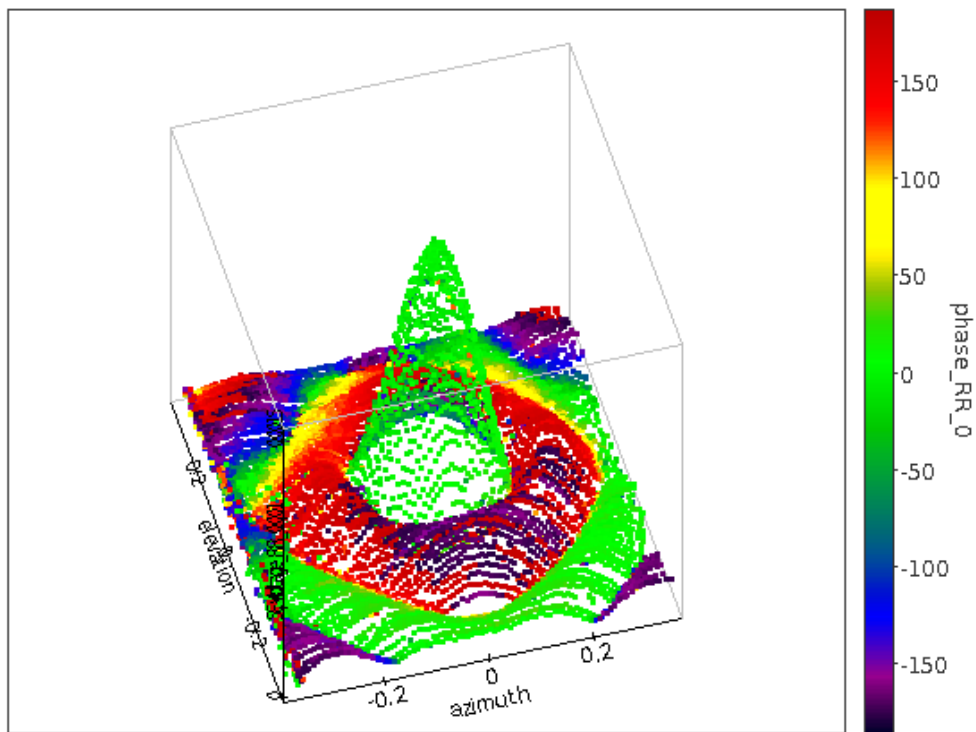


Fig 23: Plots of the Pickmere telescope beam – there are small departures from expected symmetry

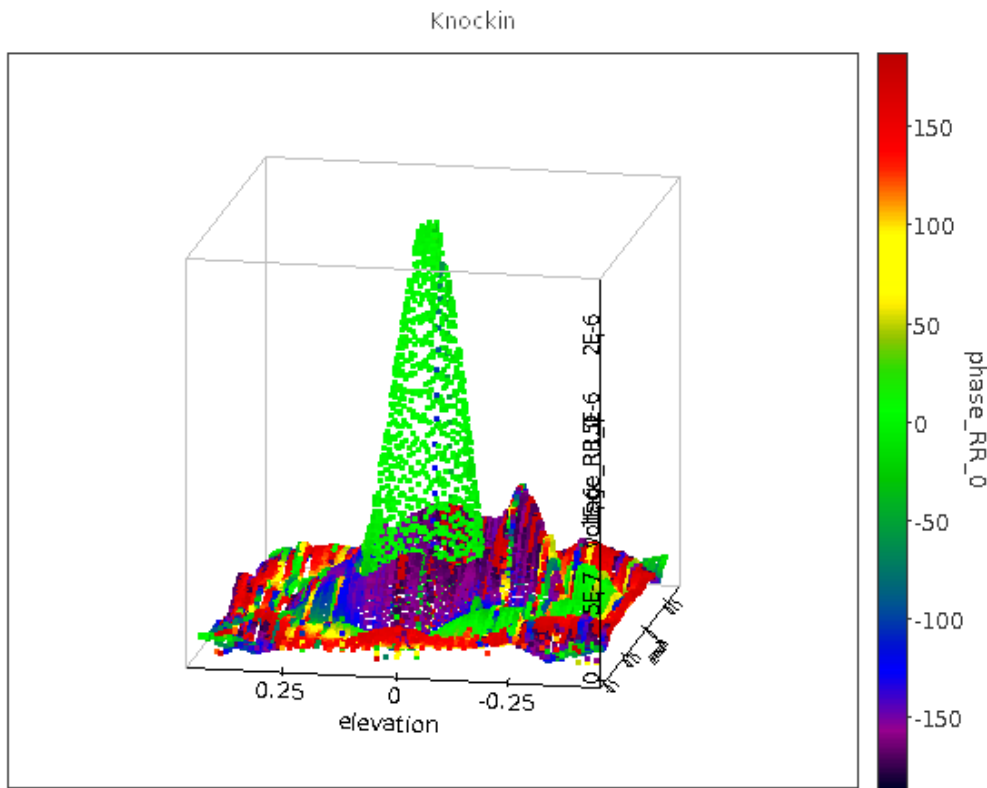
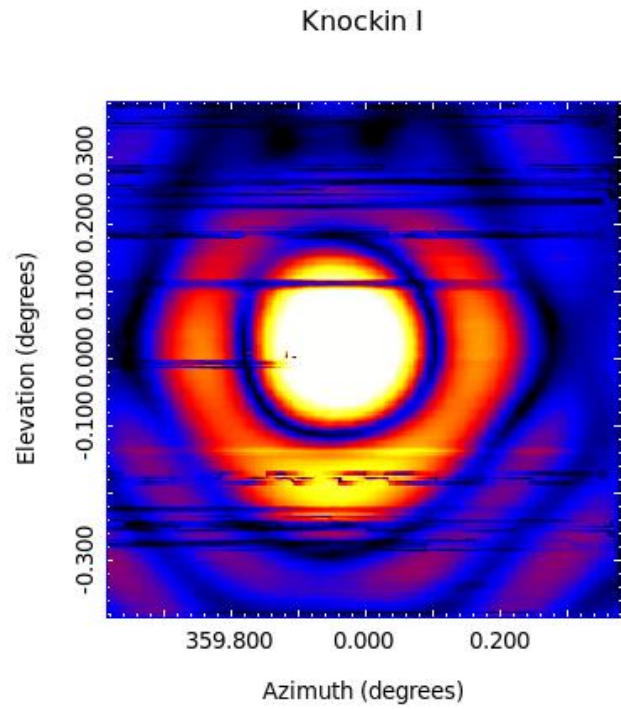
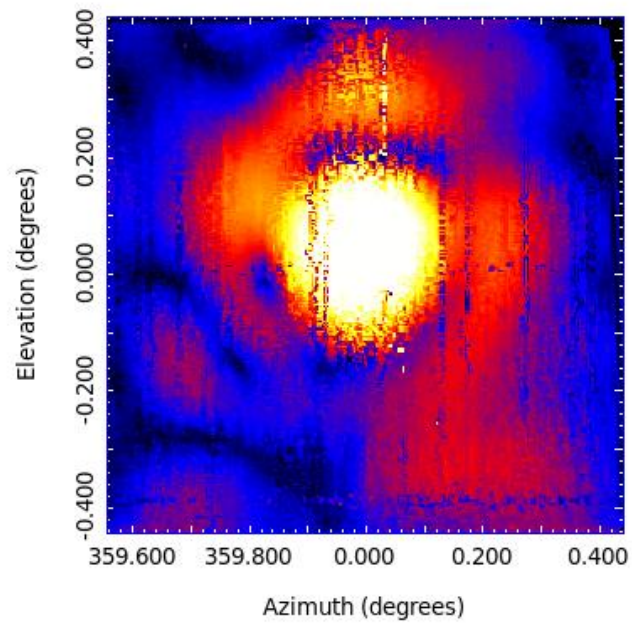


Fig 24: Plots of the Knockin telescope beam further departures from rotational symmetry can be seen

Defford I



Defford

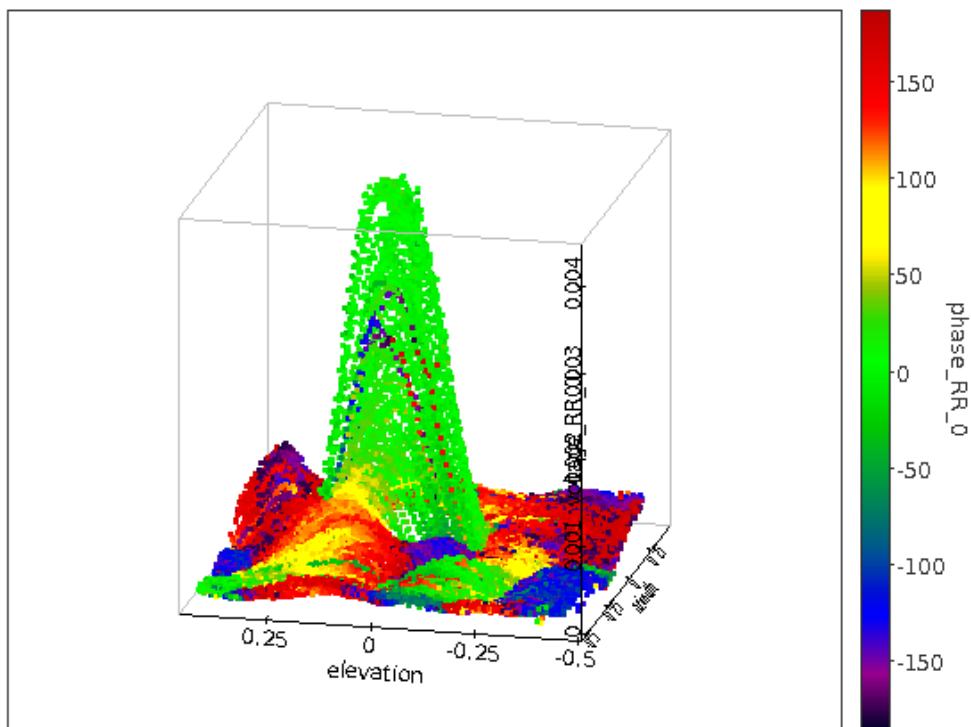
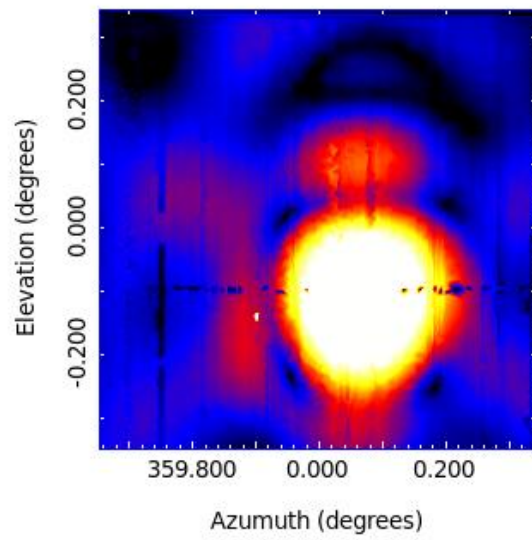


Fig 25: Plots of the Defford telescope beam – this beam is much less symmetrical than previously shown telescopes – however, this is to be expected to some extent as the antenna is of a different design

Mk2 I



MK2

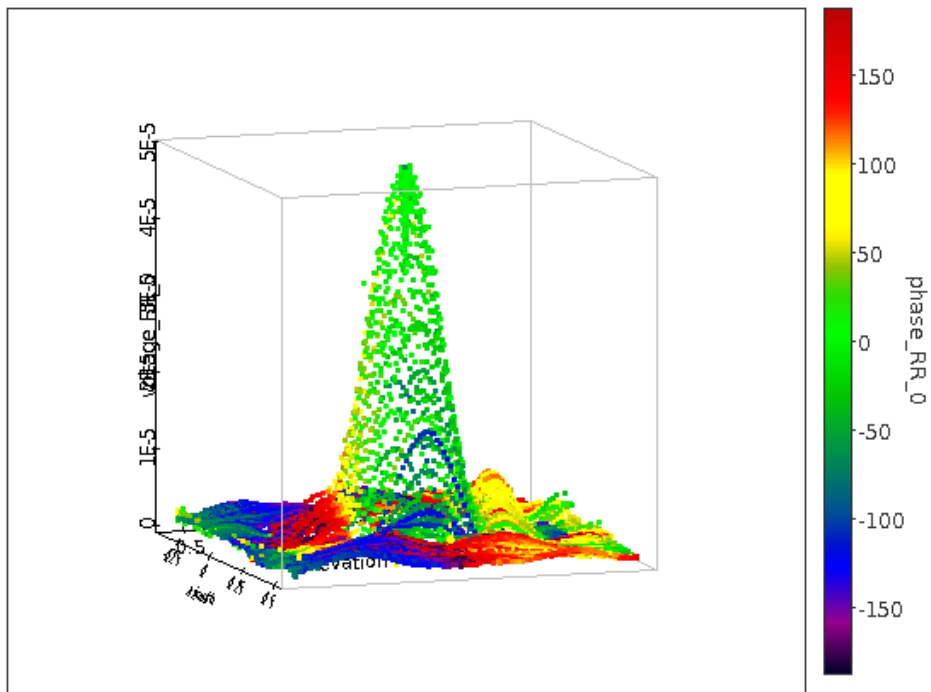


Fig 26: Plots of the MK2 telescope beam – A pointing offset from the nominal position can clearly be seen.

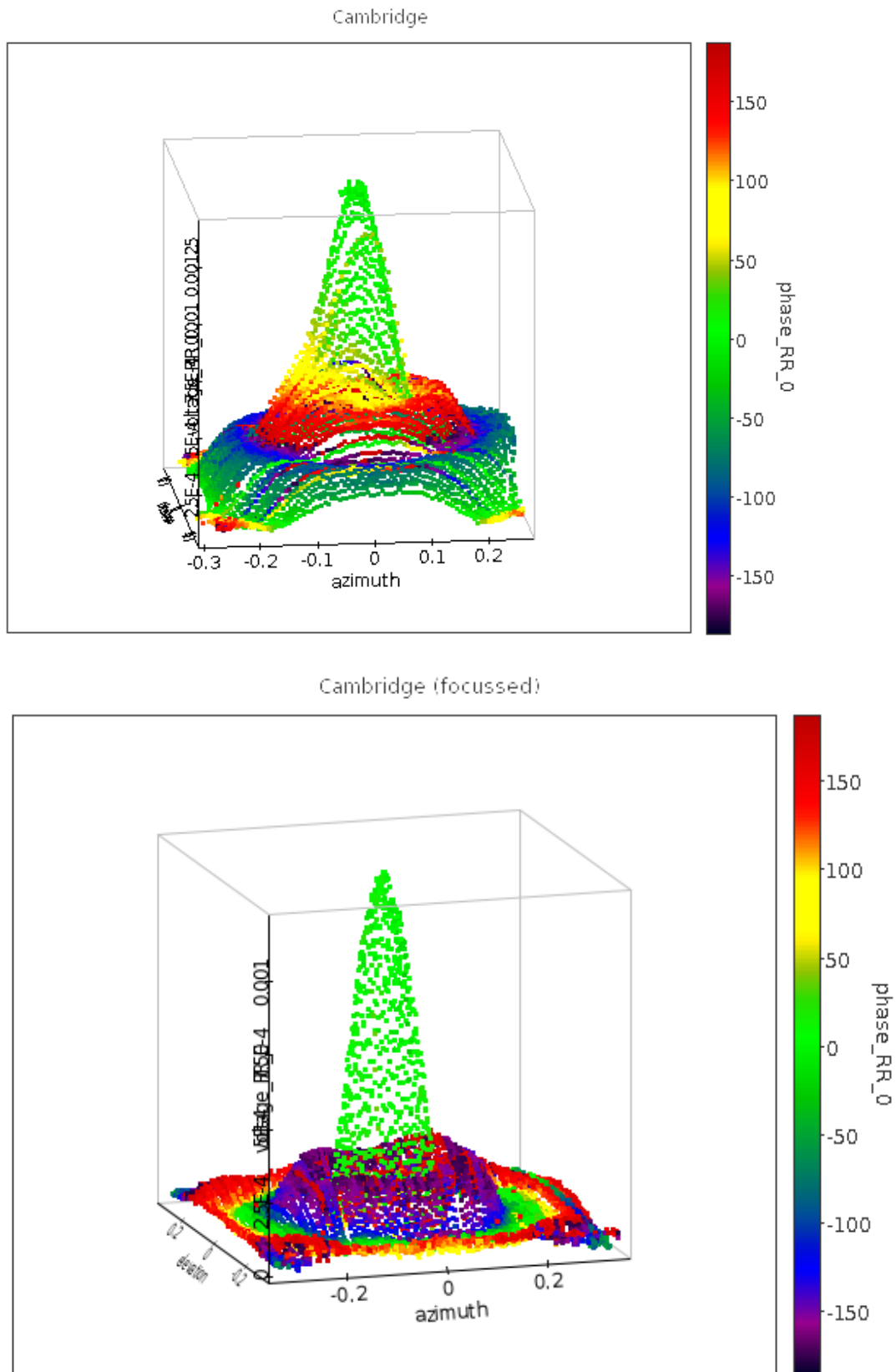


Fig 27: Plots of the Cambridge telescope beam. In the upper plot the initial measurement of the beam is displayed – this beam shows clear characteristics of the telescope not being properly focussed, as the sidelobes show a “stepped” pattern with the nulls between sidelobes being “washed out”. The lower plot shows the telescope after work to refocus it had been carried out.

Future Work

We plan to create beam maps suitable for inclusion in VPManger for all of the remaining telescopes that participate in e-MERLIN, in particular for the Lovell telescope, as well as carry out measurements of the beam at L-Band. We hope that these measured e-MERLIN telescope beams will be included with a future CASA release facilitate their use.

Now that a beam imaging pipeline is in place for the e-MERLIN system, we plan to carry out a regular program to monitor the beams to check for changes. It should then be possible to use the appropriate beam correction for each epoch of observation.

6. Summary

We have shown that precise modelling and empirical measurement of antenna voltage patterns can both provide substantial improvements over the simple analytical expressions used to date. Which to use in practice depends on the degree to which a model accurately describes the real antenna. If the differences between model and reality are small (or can be simply parameterised, for example as low-order aberrations), then the modelling approach is likely to be superior. If not, then an empirical model is mandatory, and may be simpler in the case of heterogeneous arrays of 'legacy' antennas. In either case, cross-comparison will be essential in order to understand the antenna behaviour.

The main results of these tests are as follows.

1. The primary beam responses computed from the electromagnetic simulations of ALMA antennas and receiver optics are in excellent agreement with the observed radial variation of peak flux density for a point source at different distances from the centre of the primary beam out to roughly twice the half-power radius.
2. This is a particularly encouraging result, since there are no free parameters: the model is completely determined a priori. We believe that this is the first time that a priori beam computations have been applied successfully to a modern synthesis array.
3. A simple Airy disk approximation derived simply from the observing frequency and the primary reflector diameter is hopelessly inadequate. The Airy disk approximation can be scaled by an empirical factor (currently implemented in CASA 3.4) to give much better agreement with the data at small angular offsets, but is not adequate farther out.
4. The ALMA primary beam derived by ray-tracing also fits the test data very well, provided that the tapering polynomial (which accounts for the unmodelled feed illumination pattern) is tuned appropriately.
5. Voltage patterns have been successfully derived for several e-MERLIN antennas using a modification of the holography technique on astronomical sources. The results show some asymmetries, perhaps due to misalignments, which would not be modelled by ideal antennas.
6. The derived and measured voltage patterns can be made available in a form suitable for immediate use (scaled to the exact observing frequency and rotated appropriately) once the A-projection code becomes available in CASA. This should allow a fully rigorous correction procedure to be developed and tested.